Anisotropic Radial Basis Function Methods for Continental Size Ice Sheet Simulations

Gong Cheng and Victor Shcherbakov

April 28, 2017

Abstract

In this paper we develop and implement anisotropic radial basis function methods for simulating the dynamics of ice sheets and glaciers. We test our methods on several well established benchmark tests: ISMIP-HOM B and D that correspond to a glacier size ice and modified EISMINT that corresponds to a continental size ice sheet. We illustrate the advantage of the radial basis function methods over a standard finite element method. Also we show how the use of anisotropic radial basis functions allows for accurate simulating the velocity of a large ice sheet, which was not possible with standard isotropic radial basis function methods due to large aspect ratio between ice width and ice thickness. Additionally, we implement the partition of unity method in order to improve the computational efficiency of the radial basis function methods.

1 Introduction

There is a growing interest in simulating the evolution of ice sheets and predicting their contribution to the future sea level rise [1]. Mathematical models are introduced as tools to understand the dynamic of ice sheets in the past and in the future [2]. The improvement in accuracy and efficiency of the modeling and the numerical methods are always preferable, especially in large scale and long time simulations [3, 4, 5].

The ice flow is generally described as an incompressible, non-Newtonian fluid with highly nonlinear viscosity. One accurate model of the ice dynamics is the so-called full Stokes (FS) equations for the velocity field [6, 7, 8]. The deformation of the ice body under its own weight is governed by the Glen's

flow law [9]. It relates the stress field to the strain rates as a viscous fluid and the viscosity depends non-linearly on the velocity, which introduces numerical difficulties in solving the FS equations. Moreover, the discretisation of the FS system gives rise to a saddle-point problem which requires special numerical treatments for the methods to satisfy the inf-sup condition [10], such as adding stabilization on the pressure variables [11] or using high-order finite element methods [12]. Therefore, the numerical solution of the FS equations is demanding in terms of computational time.

Many simplifications are derived for the FS equations to reduce the computational complexity. The first order Stokes model (or sometimes called Blatter–Pattyn model) is based on the assumption that the hydrostatic pressure is balanced by the vertical normal stress [13, 14], such that the horizontal gradient of the vertical velocities are neglected. The system is simplified to an elliptic problem that only contains the horizontal velocities as unknowns and the vertical velocity is recovered by solving the incompressibility equation. Other approximations are the shallow ice approximation (SIA) [15] and shallow shelf approximation (SSA) [16, 17].

These models are intercompared within several benchmark experiments during the past decade. For instance, the benchmark experiment of Ice Sheet Model Intercomparison Project for Higher-Order ice sheet Models (ISMIP-HOM) [4] and the framework of European Ice Sheet Modeling Initiative (EISMINT) [18]. In ISMIP-HOM, different Stokes approximations are compared on glacier size problems (about 10 km wide), whereas in EISMINT, the computational domains are continental size (more than 1000 km wide).

Traditional numerical methods such as finite element methods (FEM) are commonly used for solving ice sheet models since FEM can easily handle complex geometry with different types of boundary conditions. However, it has some drawbacks such as the moving boundary leads to remeshing for every time step and solving the nonlinear system requires reassembling during each nonlinear iteration. This suggests a mesh-free approach to solve the ice flow problem with free surface by using radial basis function (RBF) method [19].

In this paper, we continue the work in [19] and extend the RBF methods to solve continental size of ice sheet problems. We introduce anisotropic RBF methods which allow for easy handling of the continental ice sheet geometries, which typically have large aspect ratios. The geometry's high aspect ratio was an obstacle for standard isotropic RBFs due to the strong dependence of the shape parameter. The use of anisotropic RBFs significantly relaxes this dependance and simplifies the method's implementation. Anisotropic RBF methods have been used to solve PDEs [20, 21] but never in applications to glaciology.

The outline of the paper is as follows. The FS equations that govern the dynamics of the ice sheets and the first order Stokes model model are explained in Section 2. The RBF methods are introduced in Section 3. In Section 4, we show the numerical results obtained by the RBF methods for three different benchmark experiments. We also provide a comparison of the RBF methods with the standard FEM in terms of time-to-accuracy, i.e., we compare the execution times to achieve certain error levels. The conclusions are drawn in Section 5.

2 Ice Sheet Dynamics

Ice can behave like a fluid flow in the large scales such as glacier and ice-sheet, so the ice sheet modelings are generally inspired by fluid dynamics. It can be considered as an incompressible flow with a low Reynolds number. The stress tensor is related to the strain rate by a power law viscous rheology [6]. From Navier-Stokes equations to the full Stokes equation, the acceleration term is neglected due to the slow motion of the ice. To reach the first order Stokes equation, another simplifications are made on the stress tensor based on the assumption that the ice has a large aspect ratio and the surface is nearly flat. Therefore, the first order Stoke equation may not be very accurate comparing to the full Stokes equation at the ice margin, close to the grounding line and the calving front.

2.1 The Full Stokes Equations

The non-linear FS equations are defined by the conservation of momentum and mass

$$\begin{aligned} \nabla \cdot (\eta(\nabla \mathbf{v} + \nabla \mathbf{v}^T)) - \nabla p + \rho \mathbf{g} &= 0, \\ \nabla \cdot \mathbf{v} &= 0, \end{aligned} \tag{1}$$

where $\mathbf{v}$ is the vector of velocities $\mathbf{v} = \begin{pmatrix} v_x & v_y & v_z \end{pmatrix}^T$, ρ is the density of the ice, η is the viscosity, p is the pressure and $\mathbf{g}$ is the gravitational acceleration. A constitutive equation(so called Glen's flow law) relates the deviatoric stress tensor $\mathbf{T}^D$ and the strain rate $\mathbf{D} = \frac{1}{2}\left(\nabla \mathbf{v} + (\nabla \mathbf{v})^T\right)$ such that

$$\mathbf{D} = \mathcal{A}(T') f(\sigma) \mathbf{T}^D, \tag{2}$$

where $\mathcal{A}(T')$ is the rate factor that describes how the viscosity depends on the pressure melting point corrected temperature T'. For isothermal flow, the rate factor $\mathcal{A}$ is constant. The value of the physical parameters are given in Table 1.

The deviatoric stress tensor $\mathbf{T}^D$ is given by

$$\mathbf{T}^D = \begin{pmatrix} t^D_{xx} & t^D_{xy} & t^D_{xz} \\ t^D_{yx} & t^D_{yy} & t^D_{yz} \\ t^D_{zx} & t^D_{zy} & t^D_{zz} \end{pmatrix}, \tag{3}$$

where t^D_{xx}, t^D_{yy}, t^D_{zz} and t^D_{xy} denote longitudinal stresses and t^D_{xz}, t^D_{yz} vertical shear stresses. The function $f(\sigma)$ is called the creep response function for ice that

$$f(\sigma) = \sigma^{n-1}, \tag{4}$$

where n is the flow-law exponent factor and σ is the effective stress which is defined as the second invariant of the deviatoric stress tensor

$$\sigma = \left[(t^D_{xy})^2 + (t^D_{yz})^2 + (t^D_{xz})^2 + \frac{1}{2}\left((t^D_{xx})^2 + (t^D_{yy})^2 + (t^D_{zz})^2 \right) \right]^{\frac{1}{2}}. \tag{5}$$

The effective strain rate is defined in analogy with the effective stress such that

$$\mathbf{D}_e = \sqrt{\frac{1}{2}\operatorname{tr}(\mathbf{D}\cdot\mathbf{D})} \tag{6}$$

with the relation

$$\mathbf{D}_e = \mathcal{A}\sigma^n, \tag{7}$$

and the viscosity η defined by

$$\eta = (2\mathcal{A}f(\sigma))^{-1} = \frac{1}{2}\mathcal{A}^{-\frac{1}{n}}\mathbf{D}_e^{\frac{1-n}{n}}. \tag{8}$$

At the top surface with normal $\mathbf{n}_s$, the ice is stress free with

$$(-p\mathbf{I} + 2\eta\mathbf{D})\cdot\mathbf{n}_s = 0, \tag{9}$$

where $\mathbf{I}$ is the identity matrix.

At the base of the ice, the normal vector $\mathbf{n}_b$ and the tangential vectors $\mathbf{t}_1$ and $\mathbf{t}_2$ span the base surface such that $\mathbf{n}_b\cdot\mathbf{t}_i = 0$, $i = 1, 2$ and $\mathbf{t}_1\cdot\mathbf{t}_2 = 0$. If the ice base is frozen, the velocity $\mathbf{v}$ satisfies a no slip condition at the base

$$\mathbf{v} = 0. \tag{10}$$

An ice sliding at the base is modeled by a sliding law [22] for the tangential velocities and the normal velocity is confined to be zero by the solid bed that

$$\begin{aligned} \mathbf{t}_i\cdot(-p\mathbf{I} + 2\eta\mathbf{D})\cdot\mathbf{n}_b + \beta\mathbf{v}\cdot\mathbf{t}_i &= 0,\ i = 1, 2; \\ \mathbf{v}\cdot\mathbf{n}_b &= 0. \end{aligned} \tag{11}$$

Parameter	Value	Unit	Description
ρ	900	kg m^{-3}	Ice density
g	9.81	m s^{-2}	Acceleration of gravity
n	3	–	Flow-law exponent
$\mathcal{A}$	10^{-16}	Pa^{-3}a^{-1}	Rate factor in flow law

Table 1: The physical parameters of ice.

where $\beta \geq 0$ describes the friction coefficient at the base.

The time dependency is introduced by a kinematic boundary condition at the top surface which moves the surface $h(x, y)$ according to the surface velocities and the accumulation-ablation function a_s that

$$\frac{\partial h}{\partial t} + v_x \frac{\partial h}{\partial x} + v_y \frac{\partial h}{\partial y} = a_s + v_z, \tag{12}$$

where a_s is in the unit m/a ice equivalent. Positive values of a_s imply snowing and negative values imply surface melting.

2.2 The First Order Stokes Model

As the FS equations are complex with the highly nonlinear viscosity, these equations are often simplified to a reduced form under the assumption that the variational stress is neglected [23] due to the large aspect ratio. The conservation of momentum in (1) becomes

$$\begin{aligned}
&\frac{\partial}{\partial x}\left(4\eta\frac{\partial v_x}{\partial x} + 2\eta\frac{\partial v_y}{\partial y}\right) + \frac{\partial}{\partial y}\left(\eta\frac{\partial v_x}{\partial y} + \eta\frac{\partial v_y}{\partial x}\right) + \frac{\partial}{\partial z}\left(\eta\frac{\partial v_x}{\partial z}\right) = \rho g\frac{\partial h}{\partial x},\\
&\frac{\partial}{\partial x}\left(\eta\frac{\partial v_x}{\partial y} + \eta\frac{\partial v_y}{\partial x}\right) + \frac{\partial}{\partial y}\left(4\eta\frac{\partial v_y}{\partial y} + 2\eta\frac{\partial v_x}{\partial x}\right) + \frac{\partial}{\partial z}\left(\eta\frac{\partial v_y}{\partial z}\right) = \rho g\frac{\partial h}{\partial y},
\end{aligned} \tag{13}$$

where $h(x, y)$ denotes the surface elevation and the viscosity is written as

$$\begin{aligned}
\eta =& \frac{1}{2}\mathcal{A}^{-\frac{1}{n}}\left[\left(\frac{\partial v_x}{\partial x}\right)^2 + \left(\frac{\partial v_y}{\partial y}\right)^2 + \frac{\partial v_x}{\partial x}\frac{\partial v_y}{\partial y}\right.\\
&\left. + \frac{1}{4}\left(\frac{\partial v_x}{\partial y} + \frac{\partial v_y}{\partial x}\right)^2 + \frac{1}{4}\left(\frac{\partial v_x}{\partial z}\right)^2 + \frac{1}{4}\left(\frac{\partial v_y}{\partial z}\right)^2\right]^{\frac{1-n}{2n}}.
\end{aligned} \tag{14}$$

The vertical velocity is obtained through the vertical integration over the conservation of mass in (1) from the bottom $b(x, y)$ to a height $z(x, y)$

$$v_z(z) - v_z(b) = -\int_b^z \left(\frac{\partial v_x}{\partial x} + \frac{\partial v_y}{\partial y}\right) \mathrm{d}\xi. \tag{15}$$

The stress free boundary on the top surface is expressed in terms of the velocity gradients such that

$$\begin{aligned}\left(4\eta\frac{\partial v_x}{\partial x}+2\eta\frac{\partial v_y}{\partial y}\right)\frac{\partial h}{\partial x}+\left(\eta\frac{\partial v_x}{\partial y}+\eta\frac{\partial v_y}{\partial x}\right)\frac{\partial h}{\partial y}-\eta\frac{\partial v_x}{\partial z}=0,\\ \left(4\eta\frac{\partial v_y}{\partial y}+2\eta\frac{\partial v_x}{\partial x}\right)\frac{\partial h}{\partial y}+\left(\eta\frac{\partial v_x}{\partial y}+\eta\frac{\partial v_y}{\partial x}\right)\frac{\partial h}{\partial x}-\eta\frac{\partial v_y}{\partial z}=0.\end{aligned} \tag{16}$$

The basal sliding condition in (11) is written as

$$\begin{aligned}\left(4\eta\frac{\partial v_x}{\partial x}+2\eta\frac{\partial v_y}{\partial y}\right)\frac{\partial h}{\partial x}+\left(\eta\frac{\partial v_x}{\partial y}+\eta\frac{\partial v_y}{\partial x}\right)\frac{\partial h}{\partial y}-\eta\frac{\partial v_x}{\partial z}=-\beta v_x^{(b)},\\ \left(4\eta\frac{\partial v_y}{\partial y}+2\eta\frac{\partial v_x}{\partial x}\right)\frac{\partial h}{\partial y}+\left(\eta\frac{\partial v_x}{\partial y}+\eta\frac{\partial v_y}{\partial x}\right)\frac{\partial h}{\partial x}-\eta\frac{\partial v_y}{\partial z}=-\beta v_y^{(b)}.\end{aligned} \tag{17}$$

where $v_x^{(b)}$ and $v_y^{(b)}$ are the basal velocities along the bottom surface.

2.3 The Flow Line Model

In this paper, we implement two RBF methods in the 2D flow line model which can be considered as a cutting plane along the surface gradient. The first order Stokes equations in (13) combined with the conservation of mass in (1) are reduced to

$$\begin{aligned}4\frac{\partial}{\partial x}\left(\eta\frac{\partial v_x}{\partial x}\right)+\frac{\partial}{\partial z}\left(\eta\frac{\partial v_x}{\partial z}\right)=\rho g\frac{\partial h}{\partial x},\\ \frac{\partial v_z}{\partial z}=-\frac{\partial v_x}{\partial x},\end{aligned} \tag{18}$$

with the viscosity (using $n=3$ in Table 1)

$$\eta=\frac{1}{2}\mathcal{A}^{-1/3}\left[\left(\frac{\partial v_x}{\partial x}\right)^2+\frac{1}{4}\left(\frac{\partial v_x}{\partial z}\right)^2\right]^{-1/3}. \tag{19}$$

The horizontal velocity v_x is only determined by the conservation of momentum in (18) and the vertical velocity v_z can be computed by vertically integrating v_x from the bottom of the ice to the certain position z as in (15)

$$v_z(z)-v_z(b)=-\int_b^z\frac{\partial v_x}{\partial x}\mathrm{d}z. \tag{20}$$

The geometry of the ice bottom is confined by the bedrock and the bedrock is assumed to have no deformation during the whole simulation.

The direction of the basal velocity follows the tangential direction of the bottom surface, so the relation between the horizontal and vertical velocity at $z = b$ satisfies

$$\frac{v_z}{v_x} = \frac{\partial b}{\partial x}, \tag{21}$$

and the slip boundary condition in (17) is rewritten as

$$\eta \left(4\frac{\partial v_x}{\partial x}\frac{\partial b}{\partial x} - \frac{\partial v_x}{\partial z} \right) + \beta v_b = 0, \tag{22}$$

where

$$v_b = v_x \sqrt{1 + \left(\frac{\partial b}{\partial x} \right)^2}. \tag{23}$$

On the top surface, the stress free boundary condition is simplified as

$$\eta \left(4\frac{\partial v_x}{\partial x}\frac{\partial h}{\partial x} - \frac{\partial v_x}{\partial z} \right) = 0. \tag{24}$$

The lateral boundary conditions are given in the following ways for different cases:

1. At the ice divide, a symmetric boundary condition is imposed as

$$\frac{\partial h}{\partial x} = 0, v_x = 0. \tag{25}$$

2. The calving front boundary is introduced by balancing the depth-averaged stress with the buoyancy force

$$\eta \left(4\frac{\partial v_x}{\partial x} + \frac{\partial v_x}{\partial z} \right) = \frac{\rho g H}{2} \left(1 - \frac{\rho}{\rho_w} \right), \tag{26}$$

where ρ_w is the density of the water and the thickness of the ice is defined as

$$H(x) = h(x) - b(x). \tag{27}$$

3. The periodic boundary conditions are in pairs for the left and right boundaries, e.g. in the ISMIP-HOM benchmark experiments. The solutions from the right boundary are mapped to the left boundary.

3 Radial Basis Function Methods

In this section we introduce the concept of radial basis function (RBF) approximation, discuss the advantages of the method and improve some disadvantages. An RBF approximation can be constructed over a set of scattered nodes, where each node is associated with a basis function. The collection of basis functions forms a finite basis in the functional space. The typical choice of basis function can be found in Table 2. An important feature of radial basis functions is that they depend only on the distance between nodes in the node set. This is a valuable property since it makes the method easily applicable to high dimensional problems. Additionally, RBF methods are mesh-free and therefore suitable for problems which are defined in domains with complex geometries, such as ice sheets and glaciers.

Table 2: Commonly used radial basis functions.

RBF	$\phi(r)$
Multiquadric (MQ)	$(1+(\varepsilon r)^2)^{1/2}$
Inverse Multiquadric (IMQ)	$(1+(\varepsilon r)^2)^{-1/2}$
Inverse Quadratic (IQ)	$(1+(\varepsilon r)^2)^{-1}$
Gaussian (GA)	$e^{-(\varepsilon r)^2}$

Given N distinct scattered nodes $\underline{x} = [x_1, \ldots, x_N]$, $x_i \in \Omega \subset \mathbb{R}^d$, we can construct an RBF approximation $\tilde{u}(x)$ of a function $u(x)$ with values $\underline{u} = [u(x_1), \ldots, u(x_N)]$ defined at the nodes such that

$$\tilde{u}(x) = \sum_{j=1}^{N} \lambda_j \phi(\varepsilon||x - x_j||), \quad x \in \Omega, \tag{28}$$

where λ_j are the unknown coefficients, $\|\cdot\|$ is the Euclidean norm and $\phi(r)$ is a real-valued radial basis function. In order to determine the coefficients λ_j we collocate the approximation (28) at the node set and obtain a system of linear equations for the coefficients $\underline{\lambda}$

$$A\underline{\lambda} = \tilde{u}(\underline{x}), \tag{29}$$

where the matrix A is constructed for the following elements $A_{ij} = \phi(\varepsilon\|x_i - x_j\|)$. It has been shown [24, 25, 26] that for smooth RBFs the magnitude of the coefficients becomes unbounded as $\varepsilon \to 0$, while the values $\tilde{u}(\underline{x})$ remain well-behaved. Therefore, we prefer to transform the problem into a search of the

nodal values $\tilde{u}(\underline{x})$. For the basis functions presented in Table 2 the interpolation matrix A is non-singular for distinct node points [27]. Hence, we can write

$$\underline{\lambda} = A^{-1}\tilde{u}(\underline{x}). \tag{30}$$

Thus, we transform the problem from the search of the weights on the basis function to the search for the values of the RBF approximation on the node set.

3.1 Anisotropic Radial Basis Functions

The thickness of a continental ice sheet is relatively small in comparison with its length. The aspect ratio between the width and the thickness may in some cases be around $400:1$. Therefore, the approximation with standard RBFs fail to provide a reasonable resolution. Bayona et al. [20] and Zhao et al. [21] suggest to use anisotropic (elliptic) RBFs instead. These are the functions, which are scaled in an appropriate way to give good resolution and match the domain geometry features (see Figure 1). This can be implemented by redefining the distance between two nodes such that

$$\|x-y\|_a = \sqrt{(x_1-y_1)^2+\cdots+a^2(x_i-y_i)^2+\cdots+(x_d-y_d)^2}, \quad x,y\in\Omega, \tag{31}$$

where a is the aspect ratio in the i-th axis. Particularly, for the two-dimensional problems that we consider in this paper the vertical dimension is several orders of magnitude smaller than the horizontal dimension. Therefore, the norm can be defined as

$$\|x-y\|_a = \sqrt{(x_1-y_1)^2+a^2(x_2-y_2)^2}, \quad x,y\in\Omega\subset\mathbb{R}^2. \tag{32}$$

A suitable value of a can be inspired by the domain discretisation. Thus, the basis function ϕ is no longer a function of the Euclidean distance but a function of the scaled distance $\|\cdot\|_a$. For the brevity of future presentation we drop the subscript a and assume that all distances are defined by the scaled norm.

3.2 Kansa's Method

The RBF interpolant (28) can also be collocated on a partial differential equation (PDE) or a system of partial differential equations. This approach is known as Kansa's method [28, 29]. The non-linear First Order Stokes Equations (18) can be written in general form as a non-linear boundary

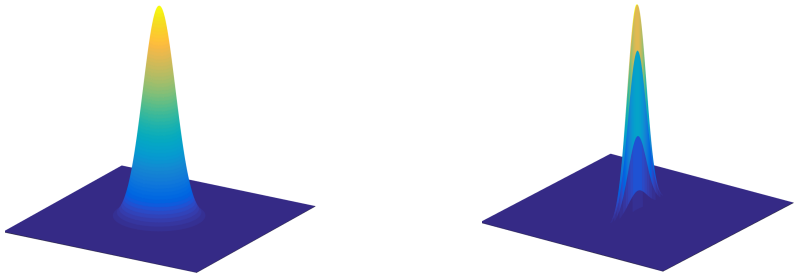

Figure 1: *Left:* A Gaussian RBF in the Euclidean norm. *Right:* A Gaussian RBF in the scaled norm. The aspect ratio $a = 50$.

value problem

$$\mathcal{P}\left[x, u(x), \mathcal{D}u(x)\right] = 0 \quad \Rightarrow \quad \begin{cases} \mathcal{P}_1 = 0, & x \in \Omega, \\ \mathcal{P}_2 = 0, & x \in \partial\Omega, \end{cases} \tag{33}$$

where $\mathcal{P}_1$ is the interior nonlinear operator, $\mathcal{P}_2$ is the boundary nonlinear operator, and $\mathcal{D}$ is a shorthand notation for differential operators, such as ∂_x, ∂_y, ∇. Collocating (33) based on (28), we obtain a nonlinear system of equations

$$P := \mathcal{P}\left[\underline{x}, \tilde{u}(\underline{x}), \mathcal{D}\tilde{u}(\underline{x})\right] = 0. \tag{34}$$

A root of the non-linear system (34) can be sought by a non-linear solver, such as Newton's method [30] or a fixed point iteration method [19], that iteratively solves a linearised problem. Thus, we arrive at a system of linear equations in the following form

$$\begin{cases} \mathcal{L}u(x) = f(x), & x \in \Omega, \\ \mathcal{F}u(x) = g(x), & x \in \partial\Omega, \end{cases} \tag{35}$$

where $\mathcal{L}$ is the linearised interior differential operator, $\mathcal{F}$ is the linearised boundary differential operator, and f, g are the right hand side functions. We seek a solution to system (35) in the form of the RBF interpolant (28). Collocating at the node points we obtain the following system of linear equations

$$C\underline{\lambda} := \begin{bmatrix} L \\ F \end{bmatrix} \underline{\lambda} := \begin{bmatrix} L_{II} & L_{IB} \\ F_{BI} & F_{BB} \end{bmatrix} \begin{bmatrix} \underline{\lambda}_I \\ \underline{\lambda}_B \end{bmatrix} = \begin{bmatrix} \underline{f}_I \\ \underline{g}_B \end{bmatrix}, \tag{36}$$

where L, F, $\underline{f}$, and $\underline{g}$ are discrete representations of the continuous quantities, and the subscripts I and B denote that the quantities are evaluated on the interior and the boundary nodes, respectively (without loss of generality, we assume that the first N_I nodes belong to the interior of Ω and the last

$N_B = N - N_I$ nodes belong to the boundary $\partial\Omega$). The matrices L and F are constructed of the elements $L_{ij} = \mathcal{L}\phi(\varepsilon\|x_i - x_j\|)$ and $F_{ij} = \mathcal{F}\phi(\varepsilon\|x_i - x_j\|)$. Relation (30) allows us to transform the problem from solving for $\underline{\lambda}$ to directly solving for $\tilde{u}(\underline{x})$.

$$\begin{bmatrix} L_{II} & L_{IB} \\ F_{BI} & F_{BB} \end{bmatrix} \begin{bmatrix} \underline{\lambda}_I \\ \underline{\lambda}_B \end{bmatrix} = \begin{bmatrix} L_{II} & L_{IB} \\ F_{BI} & F_{BB} \end{bmatrix} A^{-1} \begin{bmatrix} \tilde{u}(\underline{x}_I) \\ \tilde{u}(\underline{x}_B) \end{bmatrix} = \begin{bmatrix} \underline{f}_I \\ \underline{g}_B \end{bmatrix}. \tag{37}$$

3.3 Radial Basis Function Partition of Unity Method

The approach presented in the previous chapter is referred to as the global RBF approximation, since it is constructed over all discretisation points. Such an approach gives a highly accurate approximation, but results in a dense system of linear equations, which is computationally expensive to solve. To overcome this issue we employ a partition of unity method that allows for a significant sparsification of the linear system. Thereby, the high computational cost associated with the global method is reduced, while a similarly high accuracy is maintained [19, 31]. Moreover, a partition based formulation is well suited for parallel implementations.

The partition of unity method was first introduced for finite element methods by Babuška and Melenk in [32]. Later it was applied to RBF based formulations by multiple authors [31, 33, 34]. The main idea of the method is to subdivide the computational domain into subdomains and construct an RBF interpolant locally in each subdomain and then combine them together by the partition of unity functions, which serve as weights. Below comes the formal description of the method.

To define a partition of unity method for problem (35), we construct a set of overlapping patches $\{\Omega_k\}_{k=1}^M$ that form an open cover of the domain Ω, such that

$$\Omega \subset \bigcup_{k=1}^{M} \Omega_k. \tag{38}$$

Additionally, we construct a partition of unity $\{w_k\}_{k=1}^M$ that is subordinated to the open cover $\{\Omega_k\}_{k=1}^M$. The function w_k is compactly supported on Ω_k, and

$$\sum_{k=1}^{M} w_k(x) = 1, \quad x \in \Omega. \tag{39}$$

Thus, the RBF approximation can be written in the form of a weighted sum

of all local approximations

$$\tilde{u}(x) = \sum_{k=1}^{M} w_k(x)\tilde{u}_k(x), \quad x \in \Omega, \tag{40}$$

where $\tilde{u}_k(x)$ is a local approximation defined as

$$\tilde{u}_k(x) = \sum_{i=1}^{N_k} \lambda_i^k \phi(\varepsilon \|x - x_i^k\|), \quad x \in \Omega_k, \tag{41}$$

where N_k is the local number of computational nodes in partition Ω_k. The partition of unity weight functions can be constructed using Shepard's method [35]

$$w_k(x) = \frac{\varphi_k(x)}{\sum_{i=1}^{M} \varphi_i(x)}, \quad k = 1, \ldots, M. \tag{42}$$

In order to provide necessary smoothness of the solution we choose $\varphi_k(x)$ as a $C^2(\Omega_k)$ compactly supported Wendland's functions [36]

$$\varphi(r) = \begin{cases} (1-r)^4(4r+1), & \text{if } 0 \le r \le 1, \\ 0, & \text{if } r > 1, \end{cases} \tag{43}$$

which is scaled and shifted accordingly to fit the partition Ω_k.

An example of domain partitioning can be found in Figure 2. We use circular partitions in this application, however, it is also possible to use elliptic partitions as it was done in [34]. Note that the amount of overlap between patches should be limited in order to maintain a sparse pattern of the linear system. More overlap will lead to higher accuracy but denser linear system and, hence, higher computation costs, while less overlap will result in an opposite outcome with higher computational efficiency but low accuracy. We find that $20\% - 30\%$ overlap is appropriate. More on this matter can be found in [31].

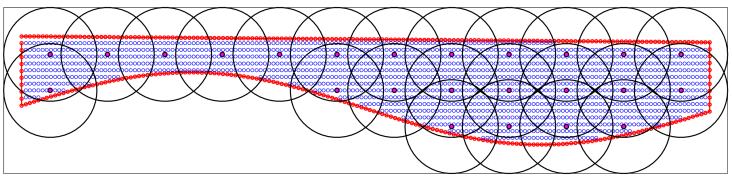

Figure 2: An example of partitioning of the domain for the ISMIP-HOM B test case.

In the experiment for the ISMIP-HOM B benchmark test our finest node set contained 1925 nodes. We applied a partitioning with 144 partitions which resulted in the following sparsity structure for the discrete differential operator (see Figure 3). In this case only 5% elements remain non-zero.

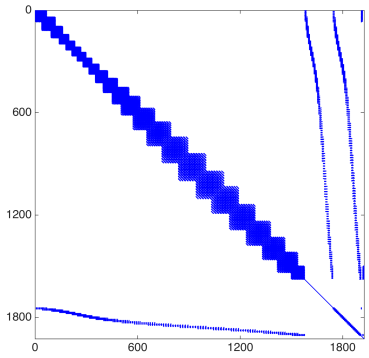

Figure 3: The sparse structure of the discrete differential operator after the application of the partition of unity method with 144 patches on a node set with 1925 nodes. Only 5% elements remain non-zero.

4 Numerical Experiments and Results

In this section we present results of numerical experiments for the ISMIP-HOM B and D benchmark tests as well as the EISMINT test on a stationary steady state domain (ice cap). We also illustrate the advantage of the radial basis function methods over the standard finite element method (with piecewise linear basis functions and an anisotropic unstructured mesh) on the ISMIP-HOM B test.

In order to construct the set of computational nodes we use a background grid that is characterized by resolutions h_x and h_y in the x- and y-axis, respectively. We select only the nodes which fall inside the domain, remove the outliers and then augment the remaining nodes with the boundary nodes.

The multiquadric basis functions are implemented and the shape parameter is chosen as the following form

$$\varepsilon = \frac{C}{h_{\text{fill}}}, \tag{44}$$

where C is some constants and h_{fill} is the fill distance that is defined such that

$$h_{\text{fill}} = \min\{h_x, h_y\}. \tag{45}$$

No analytical method of finding the value of the constant C exists. It has to be found empirically for an application on an individual basis. For our particular application we find that $C = 0.5$ is a fairly good choice. Some more detailed information on how to find C is provided in [19, 37].

The aspect ratio of RBF method in our experiments is defined as the ratio between resolutions of the grid in x- and y-directions

$$a = \frac{h_x}{h_y}. \tag{46}$$

4.1 ISMIP-HOM B

We simulate the velocity field of an ice slab that is grounded on a bedrock that has sinusoidal shape. The length of the slab is $L = 10$ km. The surface is defined as a function of the x-coordinate

$$h_s(x) = -x \tan \alpha, \quad x \in [0, L], \tag{47}$$

and has a slope $\alpha = 0.5°$ The bedrock is defined as

$$h_b(x) = h_s(x) - 1000 + 500 \sin\left(\frac{2\pi x}{L}\right), \quad x \in [0, L]. \tag{48}$$

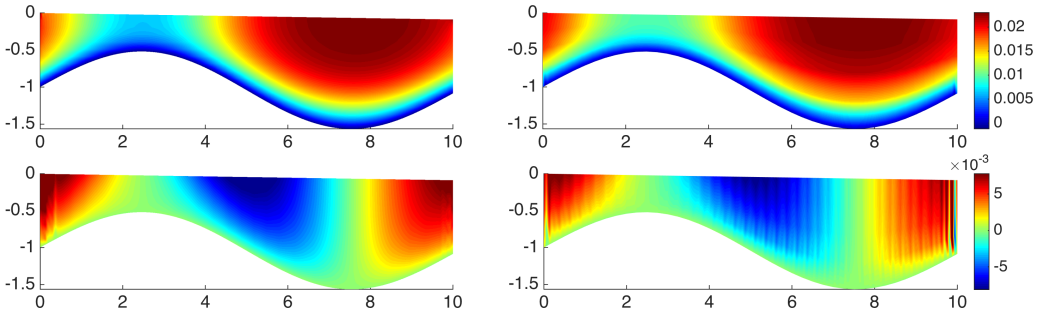

Figure 4: The horizontal and vertical velocity for the ISMIP-HOM B test measured in km/a. Horizontal velocities computed by the global RBF method (*left*) and by the FEM method (*right*) are presented on the upper panels. Vertical velocities computed by the global RBF method (*left*) and by FEM (*right*) are presented on the lower panels.

The left and right boundaries are periodical. The ice is grounded on the bedrock, meaning no slip boundary condition on the bottom. We assume that the ice surface is free of stress, i.e. this is a free surface problem.

The horizontal and vertical velocities, obtained on node sets with similar resolution, are presented in Figure 4.1. The two left panels represent the global RBF solutions, while the right panels represent the FEM solutions, which we use for comparison. We see that the horizontal velocities are resolved well by both methods, while the vertical velocities have some spurious oscillations that are larger in the FEM solution. In the RBF solution this oscillations are explained by the Runge phenomenon that occurs in the global RBF approximation. The oscillations decrease under grid refinement. The oscillations in the FEM solution are related to poor resolution and decrease under refinement.

We compare three methods: global RBF, RBF-PUM, and FEM in terms of accuracy and computational efficiency. We use a finite element solution on a fine grid with 10897 degrees of freedom as our reference solution. The absolute errors(using FEM solution on the finest mesh as a reference solution), run times, and numbers of degrees of freedom are presented in Table 3. We observe that the RBF methods give better accuracy in much shorter time. RBF-PUM is more than 8 times faster than the standard finite element method. Additionally, thanks to the high accuracy, the RBF methods need fewer nodes to reach a similar accuracy level. This is crucial for large simulations since less memory storage will be required. The reason that the FEM implementation runs slower is the necessity of matrix reassembly within the nonlinear iteration. It has been shown [38] that this procedure may severely dominate the total computational time.

Table 3: Absolute Errors (m/a) in the vertical velocity and CPU times for several different numbers of degrees of freedom for the global RBF method, RBF-PUM, and FEM for the ISMIP-HOM B benchmark test.

FEM			RBF			RBF-PUM		
Error	N	Time (s)	Error	N	Time (s)	Error	N	Time (s)
0.3353	243	2.2782	0.2535	306	0.2388	0.3467	291	0.2479
0.1528	805	8.0495	0.1574	802	1.3701	0.1365	771	0.7685
0.0492	2889	34.5913	0.0432	1992	13.7930	0.0372	1925	4.1405

In the remaining part of the paper we will present only the global RBF solution, since it is similar to the solutions obtained by RBF-PUM and FEM, however they are also implemented.

4.2 ISMIP-HOM D

In the ISMIP-HOM D benchmark test we solve for the velocity of an ice slab with slip boundary condition on the bottom. In another words, the ice is sliding on the bedrock and this is governed by a sliding law that varies as a trigonometric function of the $x-$coordinate.

Same as the ISMIP-HOM B experiment in Section 4.1 the length of the slab is $L = 10$ km. The surface elevation is defined as in (47) with a slope $\alpha = 0.1°$. The bedrock is parallel to the top surface with a constant thickness of 1000 m

$$h_b(x) = h_s(x) - 1000, \quad x \in [0, L]. \tag{49}$$

The left and right boundaries are periodic. The ice surface is free of stress. The slip boundary follows the sliding law (22) with the slip coefficient defined as

$$\beta(x) = 10^3 \left(1 + \sin\left(\frac{2\pi x}{L}\right)\right). \tag{50}$$

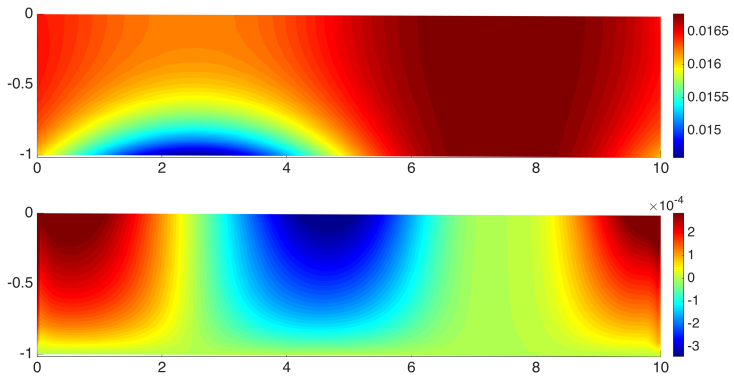

Figure 5: The horizontal (*upper panel*) and vertical (*lower panel*) velocity for the ISMIP-HOM D test measured in km/a computed by the global RBF.

Figure 4.2 illustrates the horizontal and vertical velocities. The velocity fields computed by RBF-PUM are similar to the ones presented in Figure 4.2. The RBF methods cope well with the non-linear sliding law at the base, and overall give good results. Although some same undesirable spurious oscillations in the vertical velocity towards the boundaries still may be observed. They decrease under mesh refinement.

4.3 Two-Dimensional Ice Cap

The last experiment is inspired by the EISMINT benchmark test [18], where a continental size ice sheet is built up over a long time period (∼100 000 years)

that represents an ice age cycle. The geometry at steady state introduce numerical difficulties in the spatial discretisation since the slope on the ice margin is very steep. Moreover, we would like to illustrate the clear advantage of anisotropic RBF methods for such problems over the standard isotropic RBF methods. We take the final geometry of the ice cap and simulate its velocity field. This problem is challenging for standard RBF methods because the aspect ratio is about $428:1$.

We assume no sliding on the bedrock as well as no velocity on the lateral boundaries. The ice surface is free of stress.

The horizontal velocity by the isotropic RBF method (lower panel) and the anisotropic RBF method (upper panel) are presented in Figure 4.3. We see that the standard isotropic RBF method becomes unstable and is not able at all to resolve the velocity field, while the anisotropic RBF method gives quite a good approximation to the velocity field. The reader is referred to [18] to ascertain that the presented solution is correct.

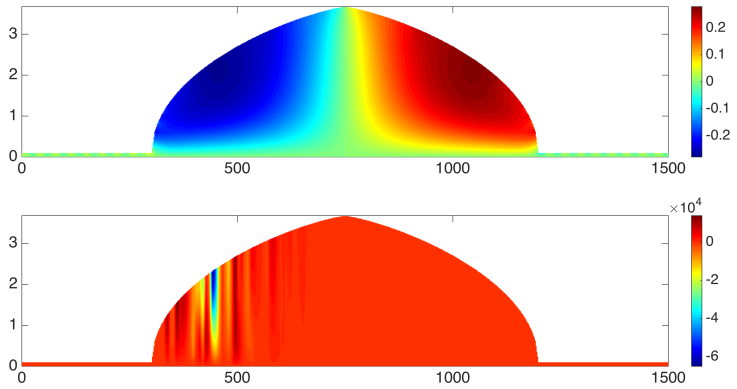

Figure 6: The horizontal velocity field for the final geometry of the EISMINT test measured in km/a computed by the anisotropic RBF method (*upper panel*) and the standard isotropic RBF method (*lower panel*).

5 Conclusion

We have implemented an anisotropic RBF method for solving different scales of ice sheet problems. A high-order approximation of the full Stokes equations is used to model the ice dynamic. We considered three different scenarios based on benchmark tests: glacial size of ice, slip basal conditions and continental size of ice sheet. The efficiency and accuracy are compared among global RBF method, RBF-PUM and FEM.

We showed that the anisotropic RBF method is suitable for different scales

of ice sheet modeling. The RBF methods are more efficient with higher accuracy than the finite element method. It becomes even more important for the applications with very high aspect ratio since special treatments are required for FEM which may lower the accuracy or increase the computational complexity. By using anisotropic RBF method, all the good features of RBF methods are preserved without extra cost. It extends RBF method to all types of ice sheet simulations.

References

[1] Rajendra K Pachauri, Myles R Allen, Vicente R Barros, John Broome, Wolfgang Cramer, Renate Christ, John A Church, Leon Clarke, Qin Dahe, Purnamita Dasgupta, et al. *Climate change 2014: synthesis report. Contribution of Working Groups I, II and III to the fifth assessment report of the Intergovernmental Panel on Climate Change*. IPCC, 2014.

[2] Robert M DeConto and David Pollard. Contribution of antarctica to past and future sea-level rise. *Nature*, 531(7596):591–597, 2016.

[3] David G Vaughan and Robert Arthern. Why is it hard to predict the future of ice sheets? *Science*, 315(5818):1503–1504, 2007.

[4] Frank Pattyn, Laura Perichon, A Aschwanden, Beate Breuer, Brigitte De Smedt, Olivier Gagliardini, G Hilmar Gudmundsson, Richard Hindmarsh, A Hubbard, Jesse V Johnson, et al. Benchmark experiments for higher-order and full stokes ice sheet models (ismip-hom). *The Cryosphere Discussions*, 2(1):111–151, 2008.

[5] F. Pattyn, C. Schoof, L. Perichon, R. C. A. Hindmarsh, E. Bueler, B. de Fleurian, G. Durand, O. Gagliardini, R. Gladstone, D. Goldberg, G. H. Gudmundsson, P. Huybrechts, V. Lee, F. M. Nick, A. J. Payne, D. Pollard, O. Rybak, F. Saito, and A. Vieli. Results of the Marine Ice Sheet Model Intercomparison Project, MISMIP. *The Cryosphere*, 6(3):573–588, May 2012.

[6] Ralf Greve and Heinz Blatter. *Dynamics of ice sheets and glaciers*. Springer Science & Business Media, 2009.

[7] Dambaru Raj Baral, Kolumban Hutter, and Ralf Greve. Asymptotic theories of large-scale motion, temperature, and moisture distribution in land-based polythermas fee sheets-a critical review and new developments. *Appl Mech Rev*, 54(3):215, 2001.

[8] Kolumban Hutter. *Theoretical glaciology: material science of ice and the mechanics of glaciers and ice sheets*, volume 1. Springer, 1983.

[9] JW Glen. The flow law of ice: A discussion of the assumptions made in glacier theory, their experimental foundations and consequences. *IASH Publ*, 47:171–183, 1958.

[10] Mats G Larson and Fredrik Bengzon. *The finite element method: Theory, implementation, and applications*, volume 10. Springer Science & Business Media, 2013.

[11] Jordi Blasco. An anisotropic pressure-stabilized finite element method for incompressible flow problems. *Computers & Mathematics with Applications*, 53(6):895–909, 2007.

[12] Tobin Isaac, Georg Stadler, and Omar Ghattas. Solution of nonlinear stokes equations discretized by high-order finite elements on nonconforming and anisotropic meshes, with application to ice sheet dynamics. *SIAM Journal on Scientific Computing*, 37(6):B804–B833, 2015.

[13] H. Blatter. Velocity and stress fields in grounded glaciers: a simple algorithm for including deviatoric stress gradients. *J. Glaciol.*, 41:333–344, 1995.

[14] F. Pattyn. A new three-dimensional higher-order thermomechanical ice sheet model: Basic sensitivity, ice stream development, and ice flow across subglacial lakes. *J. Geophys. Res.*, 108:2382, 2003.

[15] D. R. Baral, K. Hutter, and R. Greve. Asymptotic theories of large-scale motion, temperature and moisture distribution in land-based polythermal ice sheets: A critical review and new developments. *Appl. Mech. Rev.*, 54:215–256, 2001.

[16] D. R. MacAyeal. Large-scale ice flow over a viscous basal sediment: Theory and application to Ice Stream B, Antarctica. *J. Geophys. Res.*, 94:4071–4078, 1989.

[17] M. Weis, R. Greve, and K. Hutter. Theory of shallow ice shelves. *Continuum Mech. Thermodyn.*, 11:15–50, 1999.

[18] Philippe Huybrechts, T. Payne, and Intercomparison Group EISMINT. The EISMINT benchmarks for testing ice-sheet models. *Annals of Glaciology*, 23:1–12, 1996.

[19] Josefin Ahlkrona and Victor Shcherbakov. A meshfree approach to non-Newtonian free surface ice flow: Application to the Haut Glacier d'Arolla. *J. Comput. Phys.*, 330:633–649, 2017.

[20] V. Bayona, N. Flyer, G. M. Lucas, and A. J. G. Baumgaertner. A 3-D RBF-FD solver for modeling the atmospheric global electric circuit with topography (GEC-RBFFD v1.0). *Geosci. Model Dev.*, 8(10):3007–3020, 2015.

[21] Yangzhang Zhao, Qi Zhang, and Jeremy Levesley. Multilevel sparse grid collocation for linear partial differential equations, with tensor product smooth basis functions. In preparation, 2017.

[22] Christian Schoof. Coulomb friction and other sliding laws in a higher-order glacier flow model. *Mathematical Models and Methods in Applied Sciences*, 20(01):157–189, 2010.

[23] Frank Pattyn. A new three-dimensional higher-order thermomechanical ice sheet model: Basic sensitivity, ice stream development, and ice flow across subglacial lakes. *Journal of Geophysical Research: Solid Earth*, 108(B8), 2003.

[24] T. A. Driscoll and B. Fornberg. Interpolation in the limit of increasingly flat radial basis functions. *Comput. Math. Appl.*, 43(3-5):413–422, 2002. Radial basis functions and partial differential equations.

[25] E. Larsson and B. Fornberg. Theoretical and computational aspects of multivariate interpolation with increasingly flat radial basis functions. *Comput. Math. Appl.*, 49(1):103–130, 2005.

[26] Robert Schaback. Multivariate interpolation by polynomials and radial basis functions. *Constr. Approx.*, 21(3):293–317, 2005.

[27] Charles A. Micchelli. Interpolation of scattered data: distance matrices and conditionally positive definite functions. *Constr. Approx.*, 2(1):11–22, 1986.

[28] E. J. Kansa. Multiquadrics—A scattered data approximation scheme with applications to computational fluid-dynamics—I surface approximations and partial derivative estimates. *Comput. Math. Appl.*, 19(8-9):127–145, 1990.

[29] E. J. Kansa. Multiquadrics—A scattered data approximation scheme with applications to computational fluid-dynamics—II solutions to

parabolic, hyperbolic and elliptic partial differential equations. *Comput. Math. Appl.*, 19(8-9):147–161, 1990.

[30] G. E. Fasshauer. Newton iteration with multiquadrics for the solution of nonlinear PDEs. *Comput. Math. Appl.*, 43(3-5):423–438, 2002. Radial basis functions and partial differential equations.

[31] Victor Shcherbakov and Elisabeth Larsson. Radial basis function partition of unity methods for pricing vanilla basket options. *Comput. Math. Appl.*, 71(1):185–200, 2016.

[32] I. Babuska and J. M. Melenk. The partition of unity method. *Internat. J. Numer. Methods Engrg.*, 40(4):727–758, 1997.

[33] Roberto Cavoretto and Alessandra De Rossi. Spherical interpolation using the partition of unity method: an efficient and flexible algorithm. *Appl. Math. Lett.*, 25(10):1251–1256, 2012.

[34] Ali Safdari-Vaighani, Alfa Heryudono, and Elisabeth Larsson. A radial basis function partition of unity collocation method for convection-diffusion equations. *J. Sci. Comput.*, 64(2):341–367, 2015.

[35] Donald Shepard. A two-dimensional interpolation function for irregularly-spaced data. In *Proceedings of the 1968 23rd ACM National Conference*, ACM '68, pages 517–524, New York, NY, USA, 1968. ACM.

[36] Holger Wendland. Piecewise polynomial, positive definite and compactly supported radial functions of minimal degree. *Adv. Comput. Math.*, 4(4):389–396, 1995.

[37] Slobodan Milovanović and Lina von Sydow. Radial basis function generated finite differences for option pricing problems. In preparation, 2017.

[38] Josefin Ahlkrona, Per Lötstedt, Nina Kirchner, and Thomas Zwinger. Dynamically coupling the non-linear Stokes equations with the shallow ice approximation in glaciology: description and first applications of the ISCAL method. *J. Comput. Phys.*, 308:1–19, 2016.